Electron scattering studies of the ground state rotational band of ^{152}Sm

X. H. Phan,[a] H. G. Andresen,[b] L. S. Cardman,[c] J.-M. Cavedon,[a] J.-C. Clemens,[a] B. Frois,[a] M. Girod,[d] D. Gogny,[d] D. Goutte,[a] B. Grammaticos,[e] R. Hofmann,[b] M. Huet,[a] P. Leconte,[a] S. K. Platchkov,[a] I. Sick,[f] and S. E. Williamson[c]

[a]*Département de Physique Nucléaire et de Hautes Energies, Centre d'Etudes Nucléaires de Saclay, 91191 Gif-sur-Yvette, Cedex France*

[b]*Institute for Nuclear Physics, University of Mainz, 65 Mainz, Federal Republic of Germany*

[c]*Nuclear Physics Laboratory and Department of Physics, University of Illinois, Champaign, Illinois 61820*

[d]*Service de Physique Théorique et Nucléaire CEN Bruyeres-le-Chatel, 91680 Bruyeres le-Chatel, France*

[e]*Centre National d'Etudes des Telecommunications, 92130 Issy-les-Moulineaux, France*

[f]*University of Basel, Basel, Switzerland*

(Received 19 January 1988)

Electron scattering cross sections have been measured for the 0^+, 2^+, 4^+, and 6^+ levels of the ground state rotational band of ^{152}Sm for effective momentum transfers between 0.3 and 2.9 fm^{-1}. The charge and transition charge densities for these states have been inferred from a combined analysis of electron scattering, muonic atom, and Coulomb excitation data. These densities are compared to the predictions of a mean field theory that describes this nucleus by a triaxial microscopic calculation in the Hartree-Fock-Bogoliubov approximation using a density-dependent force. The densities have been determined with a precision that is sufficient for the comparison of theoretical calculations with the measured densities to be sensitive to the pairing and surface properties of the effective interaction.

I. INTRODUCTION

The microscopic description of rotational nuclei can be tested by a detailed study of the ground state rotational band of ^{152}Sm, which is considered to be a good example of a simple rigid rotor. Electron scattering is well suited for examining the spatial properties of nuclear wave functions due to the purely electromagnetic character of the reaction mechanism, and to the well-understood relationship between the measured cross section and the nuclear charge and current densities. The charge and transition charge densities of the nucleus provide the meeting ground between theory and experiment. We present here the results of high momentum transfer electron scattering experiments in which cross sections for the first four states (0^+, 2^+, 4^+, and 6^+) of the ground state rotational band of ^{152}Sm were obtained. These measurements extended the q range of the existing data sufficiently to permit the charge and transition charge densities to be determined precisely and unambiguously throughout the nuclear volume. These densities are compared with the results of a mean field theory that describes ^{152}Sm using a triaxial microscopic calculation. The potentials, collective masses, and moments of inertia used in the Bohr Hamiltonian were calculated using the Hartree-Fock-Bogoliubov (HFB) method with a density-dependent force. The predictions of this theory for the transition charge densities of the ground state rotational band in ^{152}Sm are particularly sensitive to the properties of the effective interaction. The data are also interpreted in terms of the often used, semiphenomenological rigid rotor model.

II. EXPERIMENTAL PROCEDURES

A. Saclay data

The data were collected in the HE1 experimental hall at the Saclay electron linac. Scattered electrons were analyzed using the SP900 magnetic spectrometer.[1] The focal plane detector of this spectrometer, which consists of a vertical drift chamber, two plastic scintillator planes, and a Čerenkov counter, is capable of measuring very small cross sections (as low as 7×10^{-36} cm^2/sr for the ^{152}Sm 6^+ state) because of its excellent background rejection. The energy-loss system, STRADIVARIUS (Ref. 2) was used to obtain high resolution at high beam current. For optimum momentum resolution (typically $\Delta E/E = 1\times10^{-4}$) the scattering chamber was connected directly to the spectrometer without intervening vacuum windows by the use of a sliding seal. The spectrometer acceptance solid angle ranged from 0.1 to 5.0 msr.

The beam current, which varied from 5 to 15 μA, was measured to an accuracy of 1% by two ferrite-core toroid monitors and a Faraday cup. The scattering of incident electrons with energies, E, of 251 and 500 MeV was measured for a range of scattering angles, θ, corresponding to effective momentum transfers $0.6 \le q_{\rm eff} \le 2.9$ fm^{-1}. Here we define the effective momentum transfer in the usual way,

$$q_{\rm eff} = q(1+1.16Ze^2/E\langle r^2\rangle^{1/2}) ,$$

where $q = 2E\sin(\theta/2)$, Ze is the nuclear charge, and $\langle r^2\rangle^{1/2}$ is the rms radius of the ground state charge density.

The 20 and 52 mg/cm^2 thick targets were enriched to 98.3% ^{152}Sm. By continuously wobbling these targets relative to the beam, errors due to the nonuniformity of the target thickness were minimized, and excessive heating of the target was avoided. Additional cooling of the target was provided by a supersonic jet of hydrogen gas directed at the beam spot. The relative efficiencies of the detector channels were checked by measurements of the smooth quasi-elastic spectrum from ^{12}C. The stability of the detector system was examined periodically by measurement of the ^{152}Sm elastic scattering cross section at a forward angle.

B. Mainz data

The Mainz data were obtained using the Mainz 350 MeV linac for energies between 80 and 300 MeV and scattering angles between 45° and 107°, corresponding to effective momentum transfers $0.4 \leq q_{\text{eff}} \leq 2.33$ fm^{-1}. The 180°, double focusing magnetic spectrometer of the Mainz electron scattering facility[3] was incorporated into an energy-loss spectrometer system,[4] resulting in an overall momentum resolution of $\Delta p/p = 4\times 10^{-4}$ for currents up to 50 μA on the target. The focal plane detector of the spectrometer consisted of a 300 channel overlapping plastic scintillator array in combination with Čerenkov counters for background suppression.

All ^{152}Sm cross sections were determined relative to elastic scattering from ^{12}C, a well-known reference cross section.[5] The relative thickness of the ^{152}Sm and the ^{12}C reference targets were determined with a fixed scattering angle (28°) spectrometer, which was also used for beam monitoring purposes. The targets used were enriched to 98.3% ^{152}Sm and had thicknesses of 20 and 80 mg/cm^2. To account for target inhomogeneity effects, the relative thickness variations of the targets were measured by scanning the Cu K_α x-ray absorption; the influence of the target inhomogeneity was small due to the averaging effect of the relatively large beam spot size of 5×8 mm used for the energy-loss mode of operation. Beam currents up to 15 μA could be used without additional cooling of the target; the currents were determined with an accuracy of better than 0.5% by a ferrite-core monitor, whose calibration was checked repeatedly during each measurement.

III. DATA REDUCTION AND ANALYSIS

Cross sections were extracted from the measured scattering spectra by a line-shape fitting technique,[6] which corrected for straggling, bremsstrahlung, and Schwinger radiative effects. A typical experimental spectrum and the associated line-shape fit for the high resolution ($\Delta p/p \cong 1\times 10^{-4}$) Saclay data is shown in Fig. 1. Accurate cross section extraction was more difficult for the lower resolution ($\Delta p/p \cong 4\times 10^{-4}$) Mainz data. The separation of the cross sections for the 2^+ level and the elastic scattering required a careful spectrum-fitting procedure in which the line-shape information was determined experimentally by the measurement of the well-

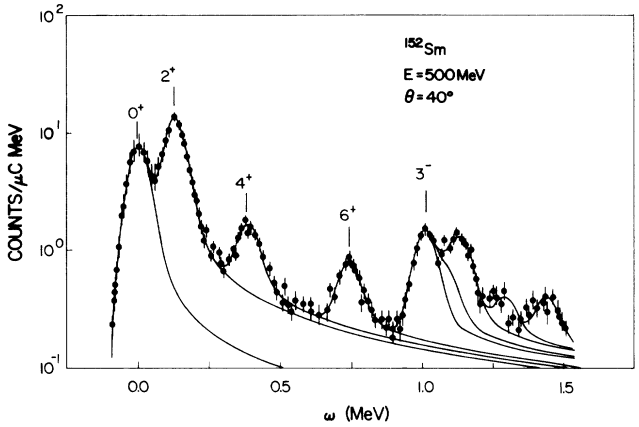

FIG. 1. A typical experimental spectrum with line-shape fit.

isolated elastic peak of ^{148}Sm under identical kinematic conditions. All data were also corrected for dead-time effects, for folding over the spectrometer acceptance, and for multiple scattering in the target. The resulting cross sections were analyzed simultaneously with previous measurements[7–10] at low and medium momentum transfers.

Results of muonic x-ray experiments[11,12] were also included in the analysis of the 0^+ and 2^+ data. These results, in the form of Barrett moments for the ground state and a generalized quadrupole moment for the first excited state, were treated as additional data points in the fit. The Barrett moment[13,14] is given by

$$\langle r^k e^{-\alpha r}\rangle = \frac{4\pi}{Ze}\int \rho_0(r) r^k e^{-\alpha r} r^2 dr \ , \tag{1}$$

where $\rho_0(r)$ is the ground state charge density; and the generalized multipole moment,[15,16] W_λ, is given by

$$W_\lambda = \sqrt{2\lambda+1}\int_0^\infty \rho_\lambda(r) r^\lambda (A + B r^m e^{-\alpha r}) r^2 dr \ , \tag{2}$$

where $\rho_\lambda(r)$ is the transition charge density for a transition of multipolarity λ. For the case of $\lambda=2$, this expression reduces to

$$W_2 = \sqrt{5}\int_0^\infty \rho_2(r) r^4 (A + B r^m e^{-\alpha r}) dr \ .$$

The constants A, B, m, and α in these equations are chosen to minimize the model dependence of the procedure of extracting a moment from the muonic, hyperfine-splitting, x-ray energies. In the case of the 4^+ state, a value of $B(E4) = (1.7\pm 0.3)\times 10^7$ e^2fm^8, which represents a weighted average of available Coulomb excitation measurements,[17–21] was included as a data point. $B(E\lambda\uparrow)$ depends on the transition charge density as follows:

$$B(E\lambda\uparrow) = (2\lambda+1)\left[\int_0^\infty \rho_\lambda(r) r^{(2+\lambda)} dr\right]^2$$
$$= 9\left[\int_0^\infty \rho_4(r) r^6 dr\right]^2 \quad \text{for } \lambda = 4 \ . \tag{3}$$

Inclusion of the Barrett moment, the generalized quadrupole moment, and the $B(E4\uparrow)$ value in the fits reduces the uncertainties in the ground state and transition charge densities inferred from the measured electron

scattering form factors. This is because these additional data provide information on the behavior of the form factor at values of the momentum transfer that are too low to be reached in a practical electron scattering experiment. The Barrett moment essentially determines the slope of the elastic scattering form factor at $q^2=0$. The generalized quadrupole moment determines the value of the $\lambda=2$ form factor at the photon point ($q=\omega$, where ω is the excitation energy of the state), while the Coulomb excitation data provide the same information for the $\lambda=4$ form factor.

The normalization of each data set depends on the measurement precision of the effective target thickness, the solid angle, and the charge collection and detection efficiencies, as well as on the method used to apply solid angle and dead-time corrections and to extract the cross sections from the experimental spectra. The absolute normalizations of the data sets reported here were determined from a self-consistent fit to the elastic scattering cross sections in which the normalizations of each data set were free parameters. This procedure works well for cases where the momentum transfer ranges of the data sets overlap substantially, and the measurements extend to low momentum transfers. The charge of the nucleus and the precisely determined muonic atom transition energies essentially fix the value and the derivative of the elastic scattering cross section at zero momentum transfer. This normalization is then transferred from data set to data set through the fitting procedure, which forces the data sets to agree where they overlap. Normalization factors for the data taken as part of this work ranged from $+0.1\%$ to $+13.3\%$. In order to ensure the consistency of the various data sets analyzed, the normalizations of previously published data were also varied during a fit of the measured elastic scattering cross sections in terms of the ground state charge density. Table I lists the normalization factors used; we found it necessary to increase both the NBS/MIT data[7,9] and the Yale data[8] by 4%. The data from the earlier Saclay/Tel-Aviv experiment[10] were decreased by 1%.

TABLE I. Data set renormalizations and quadrature errors. The cross sections and their uncertainties as listed in Table II have been obtained from the measured or published cross sections by dividing them by the normalization factors listed here; the uncertainties listed in Table II are to be increased by adding the percentage uncertainties listed here in quadrature. An additional 10% uncertainty is to be added in quadrature to the 6^+ cross sections of this experiment to account for contribution from the unresolved 0^+ state at 0.6848 MeV.

Data set	Renormalization factor	Quadrature error (%)	Ref.
Yale	0.9592	1.0	8,52
NBS-MIT	0.9640	0.0	7,9
Saclay/Tel-Aviv	1.0097	0.0	10
Mainz		0.0	This work
Saclay-79A		2.5	This work
Saclay-79B		2.5	This work
Saclay-81		2.5	This work

The excited state cross sections measured at each laboratory were corrected using the same normalization factor that was obtained from the fit to the elastic scattering data. In the case of the present data, a further correction was applied for the presence of isotopic impurities in the target. Discrepancies reported earlier[22] between the 4^+ cross sections as measured in the Saclay/Tel-Aviv experiment[10] and data from the NBS/MIT (Refs. 7 and 9) and the present experiments have been resolved by a careful reanalysis of the spectra from the Saclay/Tel-Aviv experiment. The final cross sections obtained using these procedures are listed in Table II together with relevant experimental parameters. All cross sections except those from Saclay have been corrected for the effects of multiple scattering and the angular acceptance of the spectrometer; the relevant experimental parameters for the Saclay data are listed in Table II and were accounted for in the fitting procedure used to infer the ground state and transition charge densities.

The uncertainties listed in Table II include only the effects of the identifiable sources of statistical errors. In order to account for the statistical aspects of fluctuations in the data arising from other sources (electronic drift in the beam transport and detection electronics; nonreproducibility of the spectrometer, beam, and target alignment; and instabilities in the absolute efficiencies of the detector and the beam current monitoring system), the uncertainties listed in Table I have been added in quadrature to the uncertainties quoted in Table II. The larger (10%) error added in the case of the 6^+ data accounts for the influence of the small but non-negligible admixture of the first excited 0^+ state at 0.6848 MeV, which could not be resolved in the present experiment. Estimates for the cross section for this state, based on a vibrational model and the strength of the related 2^+ state at 0.8104 MeV (which was resolved), indicate that the 6^+ cross sections will lie within the augmented error bars for $q_{\text{eff}} \geq 0.75$ fm^{-1}. A 1% uncertainty was added in quadrature to the data from the Yale experiment[8] in order to make these data statistically compatible with the overall fit to all of the data

The phase-shift code FITRAV (Ref. 23) (for the ground state) and the DWBA code HADES (Refs. 24–27) (for the excited states) were employed to extract the charge and transition charge densities. (The HADES code is discussed briefly in an appendix to this paper.) These densities were parametrized using the Fourier-Bessel series:

$$\rho_\lambda(r)=\begin{cases}\sum_{\nu=1}^{N} a_{\lambda\nu} j_\lambda(q_{\lambda\nu} r), & r \leq R_\lambda \\ 0, & r \geq R_\lambda\ ,\end{cases} \tag{4}$$

where $q_{\lambda\nu}R_\lambda$ is the νth zero of the spherical Bessel function j_λ, and R_λ is a cutoff radius beyond which the density is assumed to be zero. The densities have been normalized so that

$$Ze=4\pi\int\rho_0(r)r^2dr$$

for the ground state charge density, and $B(E\lambda\uparrow)$ is given by Eq. (3) for the transition charge densities. The transi-

TABLE II. Measured ^{152}Sm(e,e) and (e,e') cross sections. $NE-0n$ denotes $N\times10^{-n}$.

			0^+		2^+		4^+		6^+				
	E (MeV)	θ (deg)	σ (mb/sr)	$\Delta\sigma$ (%)	σ (mb/sr)	$\Delta\sigma$ (%)	σ (mb/sr)	$\Delta\sigma$ (%)	σ (mb/sr)	$\Delta\sigma$ (%)	t (mg/cm^2)	$\Delta\theta$ (deg)	$\Delta\phi$ (deg)
	251.50	31.96	7.007E −01	1.4	1.032E −01	4.3	1.326E −02	14.1	1.467E −03	74.2	19.5	0.4011	1.146
	251.50	35.97	3.360E −01	0.7	2.536E −02	3.3	7.328E −03	6.4	4.809E −04	306.9	19.5	0.4011	1.146
	251.50	43.99	6.595E −02	0.8	7.709E −02	2.9	1.104E −03	9.2	2.351E −04	27.0	19.5	0.4011	1.146
Saclay-79A	251.50	52.00	5.892E −03	1.2	3.368E −03	1.7	1.165E −04	13.8	4.034E −05	27.3	19.5	0.8594	2.865
	251.50	60.00	1.092E −03	1.9	4.192E −04	3.5	1.183E −04	6.7	1.031E −06	273.6	19.5	0.8594	2.865
	251.50	70.00	3.820E −04	2.4	1.097E −04	5.2	2.558E −05	11.0	8.015E −06	21.5	19.5	0.8594	2.865
	251.50	74.00	1.658E −04	3.1	9.820E −05	4.3	7.232E −06	17.9	3.794E −06	26.4	19.5	0.8594	2.865
	500.00	25.00							4.284E −04	24.6	19.5	0.859	2.865
	500.00	29.50	4.262E −03	2.6	2.431E −03	3.8	5.043E −04	8.8	6.556E −05	33.8	19.5	0.401	1.146
	500.00	29.50	4.051E −03	6.7	2.244E −03	8.7	5.241E −04	16.9	5.371E −05	133.6	19.5	0.344	0.344
	500.00	31.00	3.338E −03	3.2	9.582E −04	6.8	3.299E −04	11.1	2.300E −05	62.9	19.5	0.401	1.146
	500.00	33.00	2.427E −03	3.2	4.355E −04	9.4	2.750E −04	10.7	1.965E −05	58.3	19.5	0.401	1.146
	500.00	36.50	6.429E −04	3.7	3.912E −04	5.1	2.355E −05	26.8	2.521E −05	23.1	19.5	0.401	1.146
	500.00	39.00	1.356E −04	5.8	1.945E −04	5.0	1.296E −05	23.7	8.796E −06	28.9	19.5	0.401	1.146
	500.00	40.00	8.314E −05	5.1	1.408E −04	3.8	1.455E −05	13.7	6.865E −06	20.9	19.5	0.859	2.865
	500.00	42.50	2.785E −05	3.9	3.151E −05	3.7	1.716E −05	4.8	1.349E −06	26.0	52.1	0.993	4.011
	500.00	44.00	2.458E −05	3.5	1.308E −05	5.5	1.416E −05	4.5	9.053E −06	26.9	52.1	0.993	4.011
Saclay-79B	500.00	45.96	2.113E −05	4.5	9.309E −06	7.9	8.527E −06	6.9	1.459E −06	19.6	52.1	0.993	4.011
	500.00	48.00	1.375E −05	4.4	1.030E −05	5.5	2.989E −06	10.0	1.149E −06	16.8	52.1	0.993	4.011
	500.00	50.00	7.154E −06	10.1	8.184E −06	11.0	1.810E −06	29.4	4.303E −07	115.7	19.5	0.993	4.011
	500.00	50.00	6.122E −06	5.5	8.260E −06	4.7	8.345E −07	16.4	1.199E −06	12.7	52.1	0.993	4.011
	500.00	52.00	2.373E −06	7.9	4.945E −06	5.0	5.261E −07	16.7	7.989E −07	13.2	52.1	0.993	4.011
	500.00	54.00	8.094E −07	10.7	2.143E −06	5.6	4.235E −07	13.0	2.517E −06	18.8	52.1	0.993	4.011
	500.00	56.00	1.969E −07	15.1	5.612E −07	7.0	4.708E −07	7.7	1.375E −06	21.0	52.1	0.993	4.011
	500.00	58.00	1.573E −07	14.7	2.224E −07	12.4	2.779E −07	9.9	5.691E −08	31.2	52.1	0.993	4.011
	500.00	60.50	8.432E −08	16.3	1.534E −07	11.0	1.133E −07	12.4	2.350E −08	50.7	52.1	0.993	4.011
	500.00	63.50	5.542E −08	14.0	1.098E −07	8.5	1.551E −08	42.4	2.869E −08	23.8	52.1	0.993	4.011
	500.00	67.00	1.341E −08	39.4	1.160E −07	46.8	8.971E −08	57.8	7.379E −09	74.1	52.1	0.993	4.011
	500.00	25.06	4.867E −02	1.1	1.887E −02	2.0	7.552E −04	15.5	3.129E −04	26.3	19.5	0.401	1.146
	500.00	27.00	1.347E −02	1.1	9.752E −03	1.3	4.072E −04	9.1	9.229E −05	25.1	19.5	0.401	1.146
	500.00	29.00	4.705E −03	1.1	3.382E −03	1.3	4.438E −04	4.1	4.006E −05	21.0	19.5	0.401	1.146
	500.00	31.00	3.366E −03	1.3	8.739E −04	2.8	3.882E −04	4.2	2.581E −05	25.5	19.5	0.401	1.146
	500.00	33.00	2.398E −03	0.8	4.065E −04	2.5	2.303E −04	3.0	2.745E −05	12.5	19.5	0.859	2.865
Saclay-81	500.00	35.00	1.263E −03	1.3	4.218E −04	2.6	9.294E −05	5.8	2.436E −05	13.6	19.5	0.859	2.865
	500.00	38.00	2.802E −04	1.3	2.694E −04	1.3	1.260E −05	8.9	1.395E −05	7.2	19.5	0.859	2.865
	500.00	40.00	8.452E −05	1.7	1.339E −04	1.3	1.356E −05	5.0	6.181E −06	7.8	19.5	0.859	2.865
	500.00	43.05	2.574E −05	2.2	2.063E −05	2.6	1.722E −05	2.6	1.388E −06	12.4	19.5	0.859	2.865
	500.00	46.00	1.998E −05	2.2	8.713E −06	3.8	8.181E −06	3.5	1.153E −06	11.6	19.5	0.859	2.865
	500.00	49.00	9.792E −06	3.9	9.393E −06	4.1	1.546E −06	9.8	1.276E −06	10.6	19.5	0.859	2.865
	500.00	52.00	2.038E −06	6.9	4.749E −06	4.0	4.906E −07	13.4	5.750E −07	10.6	19.5	0.859	2.865

TABLE II. (*Continued*).

	E (MeV)	θ (deg)	0^+ σ (mb/sr)	$\Delta\sigma$ (%)	2^+ σ (mb/sr)	$\Delta\sigma$ (%)	4^+ σ (mb/sr)	$\Delta\sigma$ (%)	6^+ σ (mb/sr)	$\Delta\sigma$ (%)	t (mg/cm^2)	$\Delta\theta$ (deg)	$\Delta\phi$ (deg)
	81.33	46.47	4.576E +01	1.8	4.238E −01	7.2							
	81.33	58.48	8.854E +00	1.4	1.924E −01	4.0							
	81.33	70.49	1.700E +00	1.7	9.209E −02	2.5							
	81.33	82.50	3.543E −01	1.5	3.520E −02	1.8							
	81.33	94.50	1.131E −01	1.6	1.162E −02	2.1	8.834E −04	4.5					
	81.33	106.50	5.219E −02	1.4	3.318E −03	2.4	5.414E −04	4.5					
	140.51	64.48	1.111E −01	1.3	5.306E −03	6.7	1.798E −03	3.1					
	140.51	70.50	6.234E −02	1.7	2.726E −03	4.3	9.753E −04	4.0					
	140.51	76.50	3.140E −02	1.8	2.163E −03	2.3	4.875E −04	4.1					
	140.51	82.50	1.425E −02	1.7	2.039E −03	2.2	1.864E −04	4.6					
	140.51	88.50	5.308E −03	2.1	1.472E −03	2.6	4.562E −05	9.2					
	140.51	94.50	1.882E −03	2.1	9.646E −04	2.6	1.773E −05	12.4					
	140.51	100.50	7.032E −04	1.9	5.583E −04	2.2	1.340E −05	6.4					
	140.51	106.50	3.359E −04	1.9	2.576E −04	2.3	1.661E −05	4.9					
Mainz	190.23	82.50	5.461E −04	1.9	1.227E −04	3.0	5.062E −05	2.5					
	190.23	88.50	3.882E −04	2.1	4.251E −05	3.0	3.202E −05	3.0					
	190.23	94.50	2.082E −04	2.3	4.719E −05	3.2	1.236E −05	4.3					
	190.23	100.50	8.648E −05	2.3	4.353E −05	3.1	3.653E −06	7.4					
	239.27	45.84					1.325E −03	11.4					
	239.27	51.86					1.436E −04	7.7					
	239.70	70.63	5.418E −04	2.0	7.918E −05	2.9	4.069E −05	2.7					
	239.70	82.63	4.243E −05	2.8	4.966E −05	3.6	1.140E −06	19.4					
	239.70	88.63	7.902E −06	2.9	1.682E −05	3.5	2.639E −06	7.8					
	239.70	94.50	4.877E −06	2.8	3.086E −06	5.0	2.912E −06	5.4					
	299.64	73.83	9.100E −06	2.5	4.758E −06	4.9	5.364E −06	3.9					
	299.64	79.81	6.087E −06	3.1	2.565E −06	6.4	1.948E −06	7.0					
	299.64	85.89	2.224E −06	4.6	2.792E −06	6.5	2.916E −07	39.8					
	299.64	91.89	3.600E −07	15.3	1.105E −06	16.8	1.075E −07	80.0					
	251.50	25.01	8.297E +00	3.7	6.225E −01	12.2							
	251.50	30.07	1.186E +00	3.6	1.909E −01	4.7	2.007E −02	11.4					
	251.50	33.01	5.464E −01	5.1	7.660E −02	10.4							
	251.50	34.95	3.588E −01	3.5	3.559E −02	4.1							
	251.50	38.04	2.240E −01	3.5	1.414E −02	5.2	6.209E −03	6.2					
	251.50	41.05	1.356E −01	3.6	7.838E −03	5.4	3.569E −03	6.6	2.971E −04	25.0			
	251.50	45.02	5.341E −02	3.5	7.370E −03	4.3	1.083E −03	6.5	1.727E −04	26.1			
	251.50	48.98	1.664E −02	3.6	5.291E −03	4.1	2.783E −04	20.3	1.033E −04	17.4			
	251.50	52.99	4.466E −03	4.0	2.789E −03	4.3	1.100E −04	9.0	3.583E −05	26.9			
Saclay–Tel-Aviv	251.50	55.93	1.819E −03	5.5	1.538E −03	5.9	1.223E −04	14.8	1.231E −05	44.2			
	251.50	60.15	1.068E −03	5.7	4.214E −04	7.2	1.243E −04	35.3	3.646E −06	50.0			

TABLE II. (*Continued*).

	E (MeV)	θ (deg)	0^+ σ (mb/sr)	$\Delta\sigma$ (%)	2^+ σ (mb/sr)	$\Delta\sigma$ (%)	4^+ σ (mb/sr)	$\Delta\sigma$ (%)	6^+ σ (mb/sr)	$\Delta\sigma$ (%)	t (mg/cm^2)	$\Delta\theta$ (deg)	$\Delta\phi$ (deg)
	251.50	64.01	8.455E −04	6.2	1.451E −04	14.7	8.454E −05	13.8	2.931E −06	59.1			
	251.50	67.02	5.953E −04	6.1	1.099E −04	13.4	5.555E −05	14.6	3.528E −06	44.5			
	251.50	71.03	3.281E −04	5.3	1.106E −04	7.8	2.239E −05	13.2	6.797E −06	49.5			
	251.50	74.05	1.608E −04	8.2	1.006E −04	10.4	8.641E −06	35.2	5.940E −06	27.0			
	251.50	80.10	3.079E −05	15.1	4.502E −05	13.2	2.410E −06	43.1	3.192E −06	35.7			
	251.50	83.94			1.829E −05	15.9	2.941E −06	35.2	1.091E −06	71.1			
	251.50	89.01	5.125E −06	20.5	3.738E −06	25.3	3.958E −06	22.5	2.364E −07	85.1			
	251.50	94.91	4.320E −06	15.5	1.460E −06	25.1	1.987E −06	21.8	2.689E −08	173.1			
	251.50	103.96	1.473E −06	42.2	1.751E −06	41.9	5.483E −07	56.7	1.781E −07	71.7			
Yale	42.44	69.98	5.547E +01	2.1									
	42.44	69.98	5.321E +01	2.1									
	42.44	89.96	1.176E +01	2.1									
	42.44	109.94	2.673E +00	2.1									
	42.44	129.90	7.289E −01	2.1									
	42.44	139.87	3.388E −01	2.1									
	42.44	149.82	1.533E −01	2.2									
	59.99	69.97	1.232E +01	2.1									
	59.99	69.97	1.260E +01	2.1									
	59.99	69.97	1.277E +01	2.1									
	59.99	89.95	1.639E +00	2.1									
	59.99	109.93	2.565E −01	2.3									
	59.99	129.88	5.845E −02	2.8									
	59.99	139.87	3.204E −02	2.9									
NBS-MIT	49.60	93.43	4.149E +00	4.0	8.320E −02	15.0							
	60.53	93.43	1.151E +00	4.0	5.654E −02	10.0	7.054E −04	25.0					
	60.50	145.65			1.452E −03	10.0	9.969E −05	12.0					
	76.08	93.43	1.971E −01	4.0	2.044E −02	7.0	9.388E −04	6.0					
	80.38	145.65					3.112E −04	15.0					
	89.75	93.14	7.002E −02	4.0	6.120E −03	7.0	8.154E −04	5.0					
	104.95	110.79			8.392E −04	5.0	9.679E −05	7.0					
	105.68	146.01	1.743E −04	4.0			1.037E −04	0.4					
	105.71	93.46	3.921E −02	8.0	1.349E −03	7.0	4.699E −04	5.0					

tion currents associated with these charge densities have been calculated assuming that only the convection current is important. This current was calculated in the irrotational flow model by applying the continuity equation to the transition charge densities. It should be emphasized that the model uncertainties in these currents do no influence the evaluation of the present data; these currents have been calculated[28,29] to contribute less than 1% to the total cross section for low-lying collective levels for scattering angles less than 160°.

An estimate was made of the incompleteness error in the extracted densities associated with the lack of data above the maximum momentum transfer $q_{\max}$ by describing the behavior of the form factor for $q > q_{\max}$ following the prescription Rothhaas *et al.*[30] Pseudo-data, having a value of zero and an error bar extending to an upper limit given by the q dependence of the folded proton form factor, were placed at momentum transfers corresponding to the $q_{\lambda\nu}$ between $q_{\max}$ and $q_{\lambda,15}$. The model dependence introduced by these points was calculated by first making a combined fit to both the experimental and the pseudo-data to obtain a density error band. The parameters $a_{\lambda\nu}$, defined by momentum transfers beyond $q_{\max}$, were then fixed and a new, artificially smaller, error band was calculated. The difference between these two error bands was taken to be the incompleteness error. This method has been found to be reliable when $q_{\max}$ is sufficiently high.[21]

In order to eliminate the unphysical oscillations in the inferred transition charge densities for large radii that are frequently obtained from Fourier-Bessel analyses, we have constrained their asymptotic behavior by following a procedure similar to that outlined by Heisenberg.[31] The constraint assumes that the large-radius behavior of the transition charge density is exponential:

$$\rho_\lambda(r) = \frac{Ce^{-\gamma r}}{r^\beta} \quad \text{for } r > R_{\lambda a} \ , \tag{5}$$

where $R_{\lambda a}$ is the radius beyond which we wish to impose the exponential falloff. The constants C and γ are determined by matching this tail function and its derivative to the Fourier-Bessel density [Eq. (4)] at $r = R_{\lambda a}$. The fits obtained were found to be very insensitive to the choice of the exponent β; we set $\beta = 2$ for all final fits. The desired large-radius behavior was achieved by including pseudo-data, evenly spaced by ΔR from $R_{\lambda a}$ to R_λ, in the fitting procedure. Following Heisenberg,[31] this was accomplished by augmenting the chi square of the fit to the electron scattering, muonic atom, and/or Coulomb excitation data by a pseudo chi square given by the sum

$$x_p^2 = \sum_{i=1}^{M} \left[\frac{\rho(r_i) - C\exp(-\gamma r_i)/r_i^2}{w} \right]^2 , \tag{6}$$

where the number of pseudo-data points M was determined by the choice of the spacing constant ΔR: $M = (R_\lambda - R_{\lambda a})/\Delta R$; and $r_i = R_{\lambda a} + i\Delta R$. The spacing constant ΔR was chosen to be 0.2 fm; this value corresponded to about one-fifth of the wavelength of the highest frequency term in the Fourier-Bessel expansion of the density. The constant w can be used to adjust the relative weight of the pseudo-data in the fit; it was set equal to 1 for our final fits.

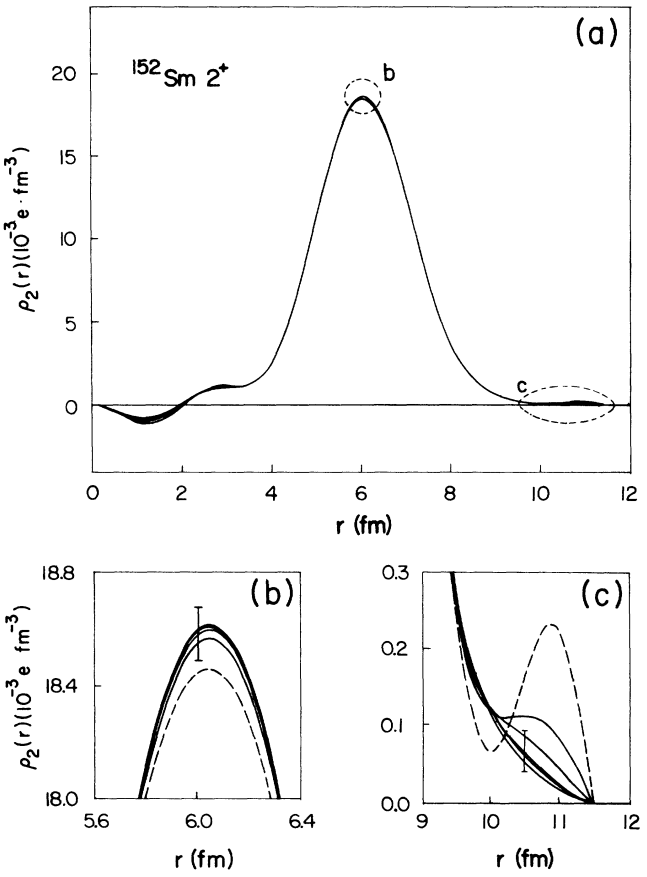

FIG. 2. (a) The $\lambda = 2$ transition density obtained with and without an r-space constraint on the density in the tail range. The sensitivity of the inferred density in the tail region (c), and at the peak of the density (b) to the choice of the matching radius $R_{\lambda a}$ are also shown. The dashed curves in (b) and (c) correspond to the case where no tail constraint was included; the other curves are for $R_{\lambda a}$ varying from 8.0 to 10.5 fm. The "error bars" in (b) and (c) show the total uncertainty in the inferred density at 6.0 fm and 10.5 fm, respectively.

Figure 2 displays the sensitivity of a typical fit to the choice of the constraint radius $R_{\lambda a}$. The density in the tail region is strongly influenced by the inclusion of the constraint, but only weakly influenced by the choice of $R_{\lambda a}$. The transition density at the peak and in the interior of the nucleus is relatively insensitive to the choice of $R_{\lambda a}$; typical variations are modest compared with the statistical and model-dependent uncertainties in the density for reasonable values of $R_{\lambda a}$ [see Figs. 2(b) and 2(c)]. The increase in χ^2 due to the inclusion of this constraint was found to be modest, indicating that the more physical, constrained density is statistically compatible with the unconstrained density. The $B(E\lambda\uparrow)$ values, however, showed a significant sensitivity to the inclusion of the tail constraint except in the case of the $\lambda = 2$ data, where the muonic atom data essentially fix $B(E2\uparrow)$. This sensitivity is due to the high weighting factor given the tail of the density in the $B(E\lambda\uparrow)$ integral [Eq. (3)]. Interestingly,

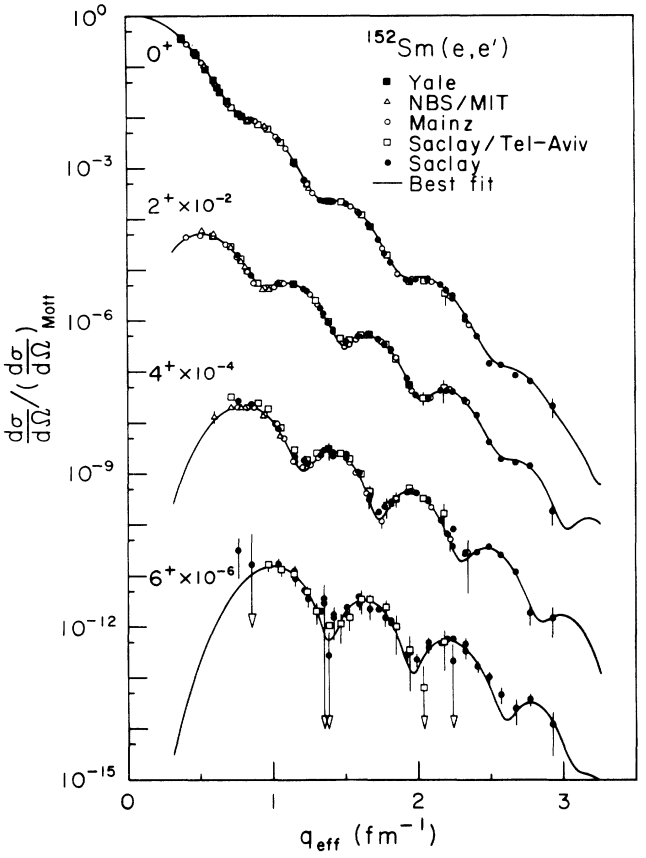

FIG. 3. Measured form factors for elastic ($\lambda=0$) and inelastic ($\lambda=2$, 4, and 6) electron scattering from the ground state rotational band of ^{152}Sm. The solid curves are based on a fit to these data using Fourier-Bessel expansions for the nuclear charge densities.

both the $B(E4\uparrow)$ and $B(E6\uparrow)$ extracted from the fit were relatively insensitive to the value of the matching radius $R_{\lambda a}$; both varied by less than their uncertainty as $R_{\lambda a}$ was varied from 8.0 to 10.5 fm.

The results of the fits to the experimentally determined form factors are shown in Fig. 3. For purposes of convenient presentation in this figure, the experimental cross sections, which were measured at a variety of beam energies, have been normalized to a beam energy of 500 MeV and plotted as a function of the effective momentum transfer. The ground state and transition charge densities obtained from this analysis are shown in Fig. 4 together with the total uncertainty including the statistical and systematic error in the measurements and the incompleteness error. In Table III we list the fitted density parameters along with the values of $R_{\lambda a}$ and R_λ. The details of the contributions of statistical, systematic, and completeness uncertainties to the overall uncertainties in the ground state and transition charge densities are also shown in Fig. 4. For the ground state density, each of these uncertainties makes roughly comparable contributions to the overall uncertainty. For the $\lambda=2$ and 4 densities, the statistical uncertainties dominate everywhere but at the peak of the density; there the contribution from the normalization uncertainty is largest. However, for the $\lambda=6$ density the statistical uncertainty dominates even in the region of the peak. As expected, the contribution of the completeness uncertainty is largest for very small radii.

IV. DISPERSIVE EFFECTS

Before comparing these densities with the predictions of Hartree-Fock-Bogoliubov theory, it is worthwhile to comment on the additional uncertainties in the densities due to the neglect of possible two-step (or dispersive) processes in our analysis of the electron scattering data. Cardman *et al.*[32] used the coupled-channel computer code ZENITH (Refs. 33–35) to examine the importance of dispersive effects on the analysis of the data from the earlier Saclay/Tel-Aviv and NBS/MIT studies of electron scattering from the ground state rotational band in ^{152}Sm. They found that the dispersive corrections to the $\lambda=0$ and $\lambda=2$ scattering were small, of order 5–10%, but the corrections for the $\lambda=4$ and $\lambda=6$ scattering, where sequential excitations of lower multipolarity can occur, were considerably larger, as much as 20% and 50% in the diffraction minimum of the $\lambda=4$ and $\lambda=6$ form factors, respectively (see Fig. 2 of Ref. 32). The application of these corrections in the analysis of the data from the Saclay/Tel-Aviv experiment resulted in changes in the inferred transition charge densities that were well contained within the error band describing the uncertainties in those densities from other sources (statistical errors, systematic errors, the incompleteness error due to the finite q range, etc.).

The quality of the data now available on electron scattering from ^{152}Sm has improved significantly; the number of data points has increased, typical statistical and systematic uncertainties have decreased, and the maximum momentum transfer measured has increased. All of these improvements have resulted in a reduction in the uncertainties in the inferred charge densities; the data now determine the shape of these densities throughout the nuclear volume. (Compare, for example, Fig. 4 with Fig. 4 of Ref. 32.) Because the charge densities inferred from a complete analysis of all presently available data are in reasonable agreement with the densities obtained from the earlier Saclay/Tel-Aviv experiment, the dispersion corrections calculated following the procedure outlined in Ref. 32 would be essentially unchanged. Comparing these corrections with the density uncertainties obtained in the analysis of the present data, we note that the uncertainty due to dispersive effects can now be estimated as *comparable* to that due to all other sources of experimental error, rather than well-contained within the error band. On the other hand, the uncertainty due to the neglect of dispersive effects is small compared with the differences between the HFB transition densities calculated using different effective forces (see Sec. IV). As a consequence one can still state with confidence that these data provide a very sensitive and precise test of the theory, but one should pay more attention to dispersive effects if the quality of the experimental data improves beyond its present high level of accuracy.

V. COMPARISON WITH THEORY

A. Introduction

We have calculated the charge and transition charge densities for ^{152}Sm using a theoretical description of nuclear structure at low excitation energy that treats both the internal and the collective aspects of nuclear motion in a unified and consistent way. The intrinsic motion of the nucleons within the nucleus is described using mean field theory.[36–38] In this approach, we begin by assuming that we have an effective nuclear Hamiltonian that characterizes the nucleus as an ensemble of independent quasi-particles moving in the mean field generated by all the nucleons. The ground state of this system is determined by solving the self-consistent HFB equations. We use the constrained HFB method to include the collective aspects of nuclear structure in the calculation. This method permits the examination of the response of the system to deformation including all effects coming from the rearrangement of the average and pairing fields. The collective coordinates are defined in a natural way as the measure of the deformations generated by the various constraints.

For our studies of ^{152}Sm, the constrained HFB procedure has been performed using a triaxial oscillator basis including eleven major shells. Initial calculations, which included only nine major shells, displayed poor convergence for the high multipole moments of the HFB wave functions. As a consequence, the strengths of the 4^+ and

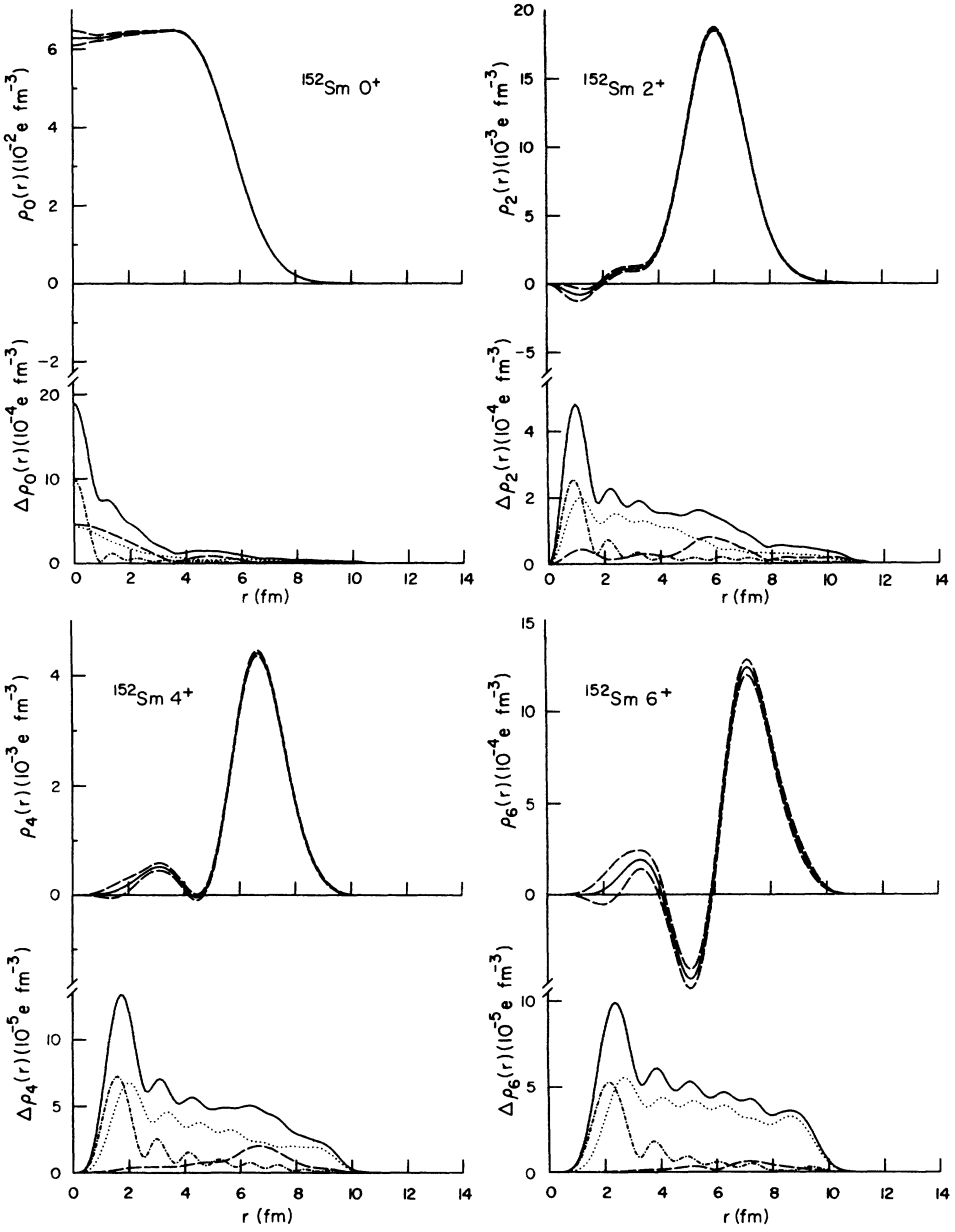

FIG. 4. The extracted density with its total error band (upper section); and the total error band (solid curve) and its breakdown in terms of contributions from statistics (· · ·), normalization uncertainty (— — —), and completeness (—·—·—·) (lower section) for the $\lambda=0$, 2, 4, and 6 members of the ground state rotational band of ^{152}Sm.

6^+ transition densities increased by 20% and 40%, respectively, when the calculation was repeated using an eleven major shell basis.[39,40] The calculation had essentially converged with this basis. A thirteen-shell calculation was performed for the values of β and γ corresponding to the minimum of the potential energy surface shown in Fig. 5; the 4^+ and 6^+ strengths increased by only 4% and 10%, respectively, relative to the eleven-shell calculation. It was felt that the eleven-shell calculation represented the best compromise between accuracy and computing time (this calculation required about ten hours on a Cray-1 to map out the potential energy surface shown in Fig. 5).

At low excitation energy, the collective motion can be described by a few parameters, namely, the quadrupole deformations. The potential energy and the collective inertia parameters are then deduced from the cranking formulae and used for solving a Schrödinger-like equation. The solution of this equation provides us with the excitation energies and the collective wave functions of the system; it also provides an approximate technique for projecting states of good angular momentum. The transition charge and current densities can then be obtained by averaging the appropriate transition operator with the collective wave functions describing the initial and final states. This approach to the collective motion of the nucleus is completely microscopic; the only adjustable parameters in the theory are those of the effective nucleon-nucleon force. The description of the nuclear dynamics is obtained without the introduction of additional phenomenological parameters to permit the adjustment of shell effects, pairing correlations, the inertia tensor, or the potential energy surface.

B. The constrained HFB method

In the constrained HFB method, we solve for a wave function $|\phi_q\rangle$ that satisfies the variational equation[10]

$$\delta(\langle\phi_q|\hat{H}-\lambda\hat{N}-\mu_0\hat{Q}_0-\mu_2\hat{Q}_2|\phi_q\rangle)=0\ , \tag{7}$$

with the conditions that

$$\begin{aligned}&\langle\phi_q|\hat{N}|\phi_q\rangle=A\ ,\\ &\langle\phi_q|\hat{Q}_0|\phi_q\rangle=q_0\ ,\\ &\langle\phi_q|\hat{Q}_2|\phi_q\rangle=q_2\ .\end{aligned} \tag{8}$$

Here, $\hat{H}$ is the effective nuclear Hamiltonian, and λ, μ_0, and μ_2 are Lagrange multipliers. The first condition ensures the conservation of the number of particles, and the last two conditions imply triaxial deformations:

$$\hat{Q}_0=\sqrt{16\pi/15}r^2Y_{20}=2z^2-x^2-y^2$$

and

$$\hat{Q}_2=\sqrt{16\pi/15}r^2(Y_{22}+Y_{2-2})=x^2-y^2\ .$$

The mean values of the operators $\hat{Q}_0$ and $\hat{Q}_2$, labeled q_0 and q_2, respectively, are collective coordinates that are related to the traditional Bohr parameters[41] β and γ

$$\beta=\sqrt{\pi/5}(q_0^2+3q_2^2)^{1/2}/A\langle r^2\rangle$$

TABLE III. Best fit parameters. The statistical uncertainties quoted in this table do not reflect the strong correlations that exist between the coefficients. $NE-0n$ denotes $N\times10^{-n}$.

	J^π	0^+		2^+		4^+		6^+
	Energy (MeV)	0.000		0.1218		0.3665		0.7067
	R_λ (fm)	10.5		11.5		12.0		12.5
	$R_{\lambda a}$ (fm)			9.5		9.5		10.5
ν	$a_{0\nu}$	$\delta a_{0\nu}$	$a_{2\nu}$	$\delta a_{2\nu}$	$a_{4\nu}$	$\delta a_{4\nu}$	$a_{6\nu}$	$\delta a_{6\nu}$
1	5.619 72$E-02$	3.7$E-06$	2.631 94$E-02$	4.7$E-05$	7.299 88$E-03$	5.1$E-05$	2.314 53$E-03$	9.9$E-05$
2	4.593 22$E-02$	1.0$E-04$	2.348 23$E-02$	2.1$E-04$	1.026 64$E-02$	7.1$E-05$	3.601 48$E-03$	1.3$E-04$
3	−3.949 99$E-02$	1.8$E-04$	−2.491 91$E-02$	1.7$E-04$	−3.389 18$E-03$	8.4$E-05$	−8.805 71$E-04$	1.4$E-04$
4	−1.840 03$E-02$	2.1$E-04$	−1.727 56$E-02$	1.7$E-04$	−7.486 22$E-03$	6.7$E-05$	−3.498 87$E-03$	9.7$E-05$
5	2.040 70$E-02$	1.1$E-04$	1.846 75$E-02$	1.4$E-04$	3.815 02$E-03$	8.1$E-05$	8.142 06$E-05$	1.2$E-04$
6	4.847 45$E-03$	1.2$E-04$	8.220 77$E-03$	1.4$E-04$	5.253 04$E-03$	8.4$E-05$	2.484 06$E-03$	8.6$E-05$
7	−6.699 20$E-03$	8.0$E-05$	−9.302 22$E-03$	1.3$E-04$	−1.225 27$E-03$	1.2$E-04$	9.872 32$E-04$	1.5$E-04$
8	−1.955 17$E-03$	1.7$E-04$	−3.587 11$E-03$	2.0$E-04$	−2.015 64$E-03$	1.0$E-04$	−6.294 88$E-04$	1.4$E-04$
9	1.066 39$E-03$	1.1$E-04$	1.762 40$E-03$	1.7$E-04$	2.957 11$E-04$	2.3$E-04$	−3.226 20$E-04$	2.8$E-04$
10	4.580 51$E-04$	4.1$E-04$	−3.330 75$E-04$	5.1$E-04$	4.426 26$E-04$		1.864 38$E-04$	
11	4.814 46$E-04$		−6.303 82$E-04$		−1.658 33$E-04$		−5.561 90$E-05$	
12	−4.651 06$E-05$		1.871 44$E-04$		1.650 38$E-05$		−4.545 99$E-05$	
13	6.235 78$E-05$		−5.495 65$E-05$		3.428 25$E-05$		6.384 22$E-05$	
14	1.328 14$E-05$		1.330 10$E-05$		−3.400 61$E-05$		−2.477 79$E-05$	
15	8.236 19$E-05$		−1.157 51$E-06$		1.908 27$E-05$		−2.930 59$E-05$	

and

$$\tan(\gamma)=\sqrt{3}q_2/q_0 ,$$

where

$$\langle r^2\rangle = x^2+y^2+z^2 .$$

Solution of the variational equation (7) for a variety of constraint conditions [Eqs. (8)] permits us to determine self-consistently the potential energy of the nucleus as a function of its deformation. This surface can be presented as a function $E(q_0,q_2)$ of the collective coordinates, or alternately, as a function $E(\beta,\gamma)$ of the more traditional Bohr parameters. The lower half of Fig. 5 displays the potential energy surface $V(\beta,\gamma)$ of the ^{152}Sm in the (β,γ) plane. The calculated potential has an axial minimum near $\beta=0.3$. This minimum is rather soft in both the β and the γ directions, implying that ^{152}Sm cannot be described well using only the HFB wave function corresponding to the minimum of the potential energy. Therefore, we have employed a dynamical treatment to define the total wave function of the nucleus as a superposition of deformed HFB wave functions within the framework of a collective model.

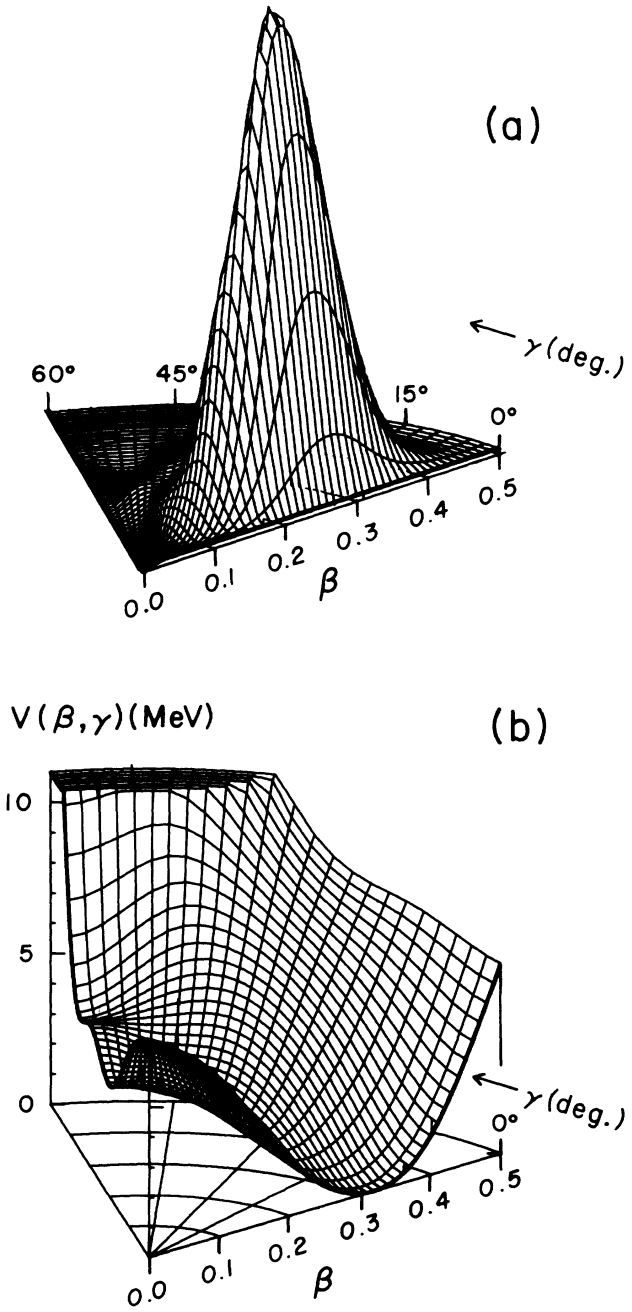

FIG. 5. (a) The collective wave function amplitudes χ_{000} for the ground state of ^{152}Sm; and (b) the potential energy surface of the ground state of ^{152}Sm as a function of the deformation parameters β and γ.

C. Nuclear dynamics

In order to treat the dynamical deformations in ^{152}Sm we have used an approximate treatment that leads to a Bohr-like Hamiltonian[42] rather than attempting to solve the more exact Griffin-Hill-Wheeler equation. We write the nuclear Hamiltonian as

$$\hat{H}= V(\beta_0,\beta_2)+\tfrac{1}{2}(B_{00}\dot{\beta}_0^2+2B_{02}\dot{\beta}_0\dot{\beta}_2+B_{22}\dot{\beta}_2^2) + \sum_{k=1}^{3}\frac{\langle I_k^2\rangle}{\mathcal{I}_k} , \quad (9)$$

where $V(\beta_0,\beta_2)$ is the collective potential[43] deduced by subtracting the zero point energy from the HFB energy $E(\beta_0,\beta_2)$. The other terms in Eq. (9) represent the collective kinetic energy, which is governed by the vibrational mass parameters B_{mn} $(m,n=0,2)$ and by the rotational moments of inertia $\mathcal{I}_x$, $\mathcal{I}_y$, and $\mathcal{I}_z$. The collective variables β_0 and β_2 are related to the Bohr parameters β and γ by $\beta_0=\beta\cos(\gamma)$ and $\beta_2=\beta\sin(\gamma)$. The inertia parameters have been calculated in the cranking approximation starting from the HFB quasi-particle wave functions.[44]

D. Transition charge densities

In $\beta_0\beta_2$ collective space the total wave function has the explicit form

$$|nIM\rangle = \int \sum_{K=0}^{I} \alpha_{IK}\chi_{nIK}(\beta_0,\beta_2) \times[D^I_{MK}(\Omega)+(-1)^K D^I_{M-K}(\Omega)] \times R(\Omega)\phi_{\beta_0\beta_2}(\mathbf{x}_i)d\beta_0 d\beta_2 d\Omega , \quad (10)$$

where I is the total angular momentum, K is its projection on the intrinsic z axis, and n is an index used to label the nuclear state ($n=0$ is the ground state, $n=1$ the first excited state, etc.). D^I_{MK} is the Wigner D matrix and R is the rotation operator, which depends on the three Euler angles between laboratory and the intrinsic axes. χ_{nIK} represents a purely collective wave function that depends only on the shape variables; it includes the metric

$$[(B_{00}B_{22}-B_{02}^2)\mathcal{I}_x\mathcal{I}_y\mathcal{I}_z]^{1/4} .$$

The HFB wave function ϕ depends on the nuclear variable x_i $(i=1,A)$, as well as on the shape parameters β_0

and β_2. Note that ϕ does not depend explicitly on I and K (in the adiabatic approximation). The integration over Ω in Eq. (10) projects states of good angular momentum, while the integration over β_0 and β_2 incorporates the dynamics of the vibrational degree of freedom.

The Bohr Hamiltonian of Eq. (9) is determined completely by the seven functions of β_0 and β_2 that can be calculated from the self-consistent HFB approach. The resolution of the Borh Hamiltonian has been performed using Kumar's code.[45] The resulting collective wave function $\chi_{000}(\beta_0,\beta_2)$ describing the ground state of ^{152}Sm is shown as a function of the Bohr parameters β and γ in the upper half of Fig. 5. The validity of the force used in the HFB calculation can be tested by comparing the excited state spectrum obtained from the diagonalization of the solution to Eq. (9) with experimental spectra. More detailed tests are provided by a comparison of the transition charge densities obtained from these collective wave functions with experimentally determined transition charge densities.

The transition charge density is defined as

$$\langle n'I'M' \mid \hat{\rho}(\mathbf{r}) \mid nIM \rangle , \tag{11}$$

where

$$\hat{\rho}(\mathbf{r}) = \sum_i \delta(\mathbf{r}-\mathbf{x}_i)$$

is the point proton charge operator. Specializing to the case of even-even rotational nuclei, transitions may take place between the ground state ($I=K=0$) and the rotational states $I=2,4,6$ and K even.

In this case the transition density can be written as

$$\langle nIM \mid \hat{\rho}(\mathbf{r}) \mid 000 \rangle = \frac{Y_{IM}(-1)^M}{\sqrt{2I+1}} \sum_{K=0}^{+I} \chi_{IK}(\beta_0,\beta_2) \frac{\rho_{IK}^{\beta_0\beta_2}(r)+\rho_{I-K}^{\beta_0\beta_2}(r)}{\sqrt{1+\delta_{K0}}} \chi_{000}(\beta_0,\beta_2) d\beta_0 d\beta_2 , \tag{12}$$

with $\rho_{IK}^{\beta_0\beta_2}(r) = \int \rho_{\beta_0\beta_2}(\mathbf{r}) Y_{IK}(\Omega) d\Omega$, where $\rho_{\beta_0\beta_2}(\mathbf{r})$ is the spatial HFB charge density folded with the finite size of the proton and neutron and corrected for center-of-mass effects.

Some approximations were invoked at this point to avoid the complete and very difficult calculation of this expression. The first approximation was the assumption of a sharp angular overlap between the HFB wave functions. This approximation has been justified by Zaringhalam and Negele[46] for well-deformed nuclei. The second approximation is similar to the first, but concerns the vibrations; we assume that the overlap between ϕ_q and $\phi_{q'}$ is sharp. However, we partially account for the finite size of the overlap by including a second-order correction to the nonlocality.

The results presented here are based on the Gogny $D1$ effective force.[47] Its parametrization includes two finite-range central components and a density-dependent term. This force is suitable for a correct and simultaneous treatment of both the mean field and the pairing field in the HFB framework. Mean field and dynamical calculations based on the HF, HF-RPA, and HFB approximations have been performed using this force over the last few years. The functional form of the force is given by[47]

$$\begin{aligned} V_{ij}^{\text{eff}}(\mathbf{r}_i-\mathbf{r}_j) = & \sum_{k=1}^{2} (W_k + B_k P_\sigma - H_k P_\tau - M_k P_\sigma P_\tau) e^{-(\mathbf{r}_i-\mathbf{r}_j)^2/\mu_k} + t_0(1+x_0 P_\sigma)\rho^\alpha \left[\frac{\mathbf{r}_i+\mathbf{r}_j}{2}\right] \delta(\mathbf{r}_i-\mathbf{r}_j) \\ & + iW_{LS}(\sigma_i+\sigma_j)(\overleftarrow{\nabla}_i-\nabla_j)\delta(\mathbf{r}_i-\mathbf{r}_j)(\overrightarrow{\nabla}_i-\nabla_j) , \end{aligned} \tag{13}$$

where P_σ and P_τ are the spin and isospin exchange operators, and the values of the adjustable parameters in the force are given in Table IV.

We have been able to improve the pairing and surface properties of the $D1$ force by comparisons between calculations using this force and the results of a variety of experiments. The nuclear matter properties of the earlier and newly obtained parametrizations (labeled $D1$ and $D1SA$, respectively, in Table V) show relatively small differences. Briefly the new $D1SA$ parametrization leads to smaller pairing correlations than the $D1$ force [see Fig. 6(a)] and it exhibits a smaller surface energy coefficient. This fine-tuning of the surface energy coefficient has led to the prediction of fission barrier heights with correct magnitudes in the actinide nuclei.[48] In addition, the $D1SA$ force reproduces more accurately the experimental odd-even mass differences for the tin isotopes; the $D1$ force leads to a binding energy difference that is 300 keV too large. This overestimates was initially thought to be desirable because one expects the quasi-particle vibration coupling to lower the binding energy difference. One may consider that the effect of this coupling has been taken into account in a phenomenological manner by the adjustments of the parameters in the $D1SA$ force. We find that collective inertia parameters calculated using the $D1SA$ force for ^{152}Sm are larger than those calculated with the $D1$ force [see Figs. 6(b) and (c)]. This surprisingly large modification of the inertia parameters is due mainly to the adjustment of the pairing correlations of the effective two-body force.

Using the formalism developed above, we have calculated the wave functions and transition densities for the ground state and low-lying excited states of ^{152}Sm using both the $D1$ and $D1SA$ forces. The results for the energies of these states are shown in Fig. 7 and compared with the experimental values. The improvement when passing from $D1$ to $D1SA$ force is clear. The lowering of the energies of the rotational states is due to the increase

TABLE IV. Effective force parameters. See Eq. (13) and Ref. 44 for the definition of the effective force.

Term	Parameter	Force *D1*	Force *D1SA*
Central	μ_1 (fm)	0.7	0.7
	μ_2 (fm)	1.2	1.2
	W_1	−402.40	−1728.5
	W_2	−21.30	106.14
	B_1	−100.00	1300.0
	B_2	−11.77	164.6
	H_1	−496.2	−1834.1
	H_2	37.27	167.95
	M_1 (MeV)	−23.56	1405.8
	M_2 (MeV)	−68.81	−226.43
Density dependent	t_0 (MeV)	1350	1390.5
	x_0	1	1
	α	$\frac{1}{3}$	$\frac{1}{3}$

of the moments of inertia as well as the increase of the mass parameters between the *D1* and *D1SA* forces. This result confirms the importance of rotation-vibration coupling in ^{152}Sm, as would be expected from the relative softness of the potential energy surface for β and γ deformations. Figure 8 displays the calculated transition charge densities for the ground state rotational band together with the densities determined by the present experiment. Results for the ground state charge density are shown in greater detail in Fig. 9. Again the improvement obtained by the use of the *D1SA* force is evident. The level of improvement is surprising considering the small adjustment between these two forces, and provides clear evidence for the sensitivity of these data to the pairing correlations.[49] Nevertheless, some disagreements remain between experiment and theory for the 6^+ state, where there is a lack of strength in the surface.

The link between the transition charge densities and the effective force used in the HFB equation is nontrivial; it is achieved only through the use of several approximations including the mean field approximation and an approximation to the Griffin-Hill-Wheeler equation as well

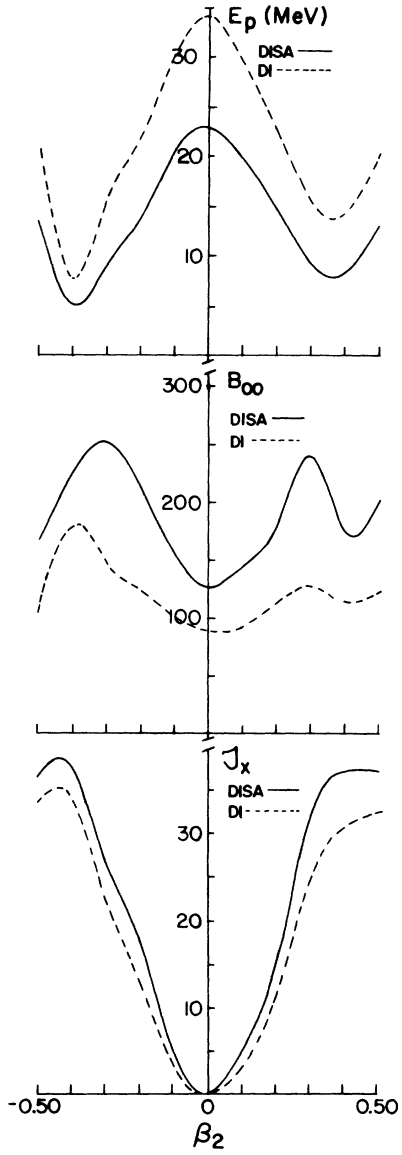

FIG. 6. (a) The total pairing energy E_p; (b) the collective mass B_{00}; and (c) the inertial moment $\mathcal{T}_x$ calculated for ^{152}Sm using the *D1* and *D1SA* forces, as functions of the deformation parameter β.

TABLE V. Nuclear-matter properties of the effective force. See Eq. (13) and Ref. 44 for the definition of the effective force.

Property	Parameter	Force *D1*	Force *D1SA*
Spin orbit	W_{LS} (MeV)	−130	−130
Volume energy	a_v (MeV)	−16.3	−16.0
Saturation momentum	k_f (fm^{-1})	1.35	1.35
Effective mass	M^*/M	0.67	0.70
Compressibility	K_∞ (MeV)	228	209
Surface coefficient	a_s (MeV)	20.2	19.0

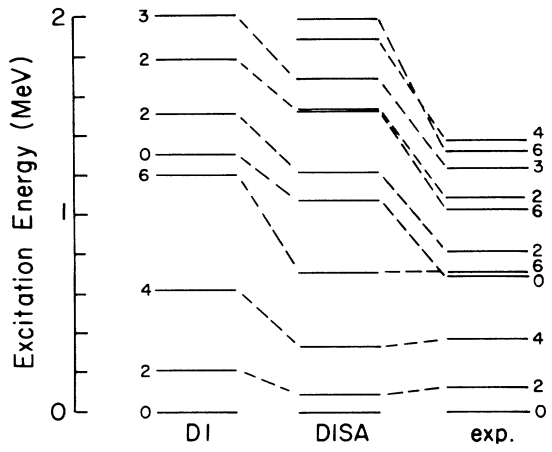

FIG. 7. Energy levels for ^{152}Sm calculated using the $D1$ and $D1SA$ forces together with the experimentally determined spectrum.

as the use of the cranking approximation for the calculation of the inertial masses. However, these results display the sensitivity of the dynamical response of the nucleus to a small change in the effective force and the crucial importance of a careful treatment of the pairing correlations and surface properties for a precise description of rotational nuclei.

VI. CONCLUSION

We have measured electron scattering cross sections for the 0^+, 2^+, 4^+, and 6^+ levels of the ground state rotational band of ^{152}Sm. The experimental data cover a momentum transfer range up to $q_{max}=2.9$ fm^{-1}, and complement data available from previous measurements; the number of cross sections measured at low and intermediate momentum transfer has increased, and the experimental uncertainties have been decreased. A new region at high momentum transfer has been explored, permitting the accurate determination of the charge and transition charge densities throughout the nuclear volume. These densities have been inferred from a combined analysis of our data and data from previous electron scattering, muonic x-ray, and Coulomb excitation experiments. Our estimate of the uncertainties associated with these densities includes both the experimental errors and the model dependence due to the finite q_{max}.

These experimentally determined densities have been used as a testing ground for the Hartree-Fock-Bogoliubov approach to the microscopic description of nuclear deformations. Due to the relative softness of ^{152}Sm against β and γ deformation, it is not possible to describe the intrinsic structure of this nucleus with a single Slater determinant. Therefore, the effects of nuclear dynamics have been incorporated through a diagonalization of the Bohr Hamiltonian for quadrupole excitations.

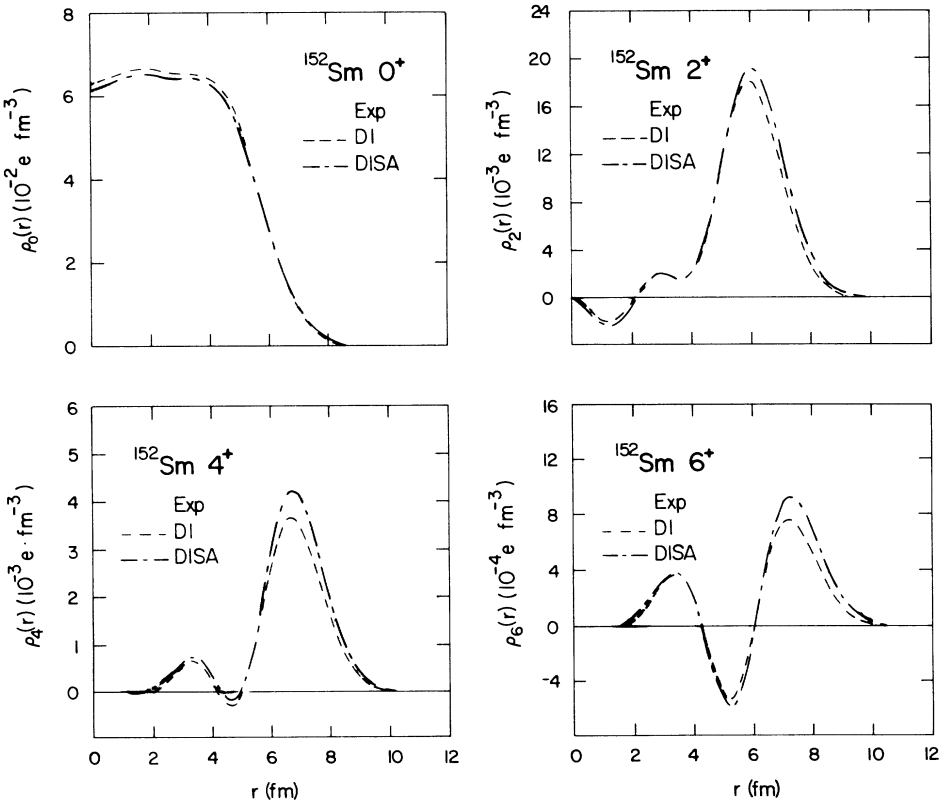

FIG. 8. The experimentally determined ground state and transition charge densities for the first four states of the ground state rotational band. Also shown are the theoretical predictions obtained using the $D1$ (— — —) and $D1SA$ (—·—·—·) effective interactions.

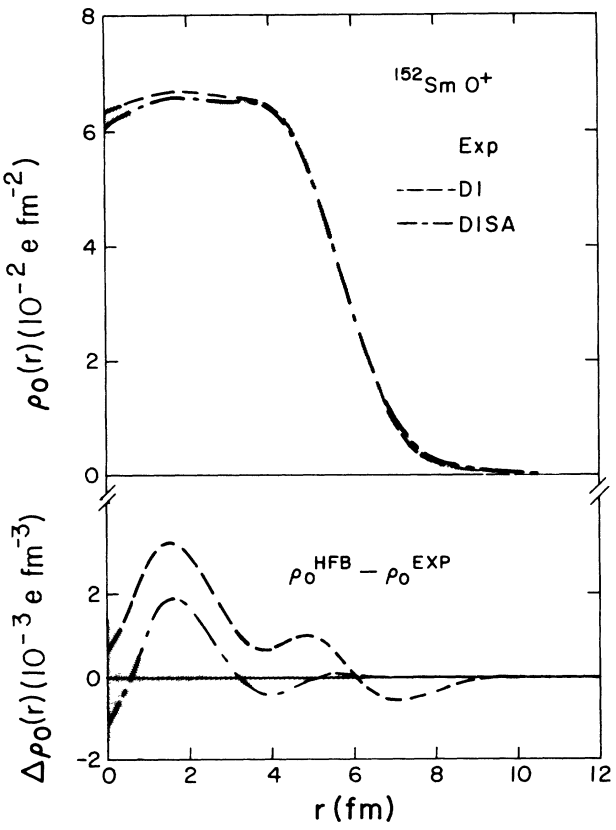

FIG. 9. The experimentally determined ground state charge density for ^{152}Sm and its uncertainty compared with the densities calculated using the *D*1 and *D*1*SA* effective interactions (a). Also shown are the differences between the experimental and theoretical densities (b).

The inertia parameters and potential energy surface of this Hamiltonian have been deduced from constrained Hartree-Fock-Bogoliubov calculations performed in a triaxial oscillator basis including eleven major shells. The theoretical predictions for the measured densities are very sensitive to the pairing and the surface properties of the effective force.

The comparison of experiment with theory shows that microscopic HFB calculations using an effective density-dependent interaction give a good description of the ground state rotational band of ^{152}Sm. These results demonstrate that mean field theory can now provide a highly accurate description of deformed nuclei using the same density-dependent force that has proven to be successful in describing spherical nuclei.

ACKNOWLEDGMENTS

This work was supported, in part, by the U. S. National Science Foundation under Grants NSF PHY 86-10493 and NSF INT 12952. We thank K. Kumar for providing the computer program used to solve the Bohr Hamiltonian. Two of us (L.S.C. and S.E.W.) would like to thank the laboratory and staff at Saclay for their kind hospitality during the course of this experiment.

APPENDIX A: THE DWBA CODE HADES

The DWBA code HADES (high-accuracy distorted-wave electron scattering) calculates the electric and magnetic transition amplitudes for elastic and inelastic electron scattering. For the calculation of the small cross sections typical of high electron energies or large momentum transfers, the numerical accuracy of distorted-wave calculations must be optimized carefully because of the slow convergence of the partial wave summations for the long-range electromagnetic interaction. The commonly used reduction technique[50] requires very high numerical accuracy for the calculation of each partial wave contribution to the transition amplitudes.[27] HADES improves on this approach by the repeated application of convergence enhancement techniques.[27] Using the standard calculation parameter set included in HADES, cross sections can be calculated for multipoles $\lambda \leq 10$ with a numerical accuracy of better than 1% for momentum transfers up to 7 fm^{-1} (the code has been tested for beam energies up to 800 MeV in combination with a backward scattering angle of 120°). The HADES code can be operated with or without consideration of the mass of the electron; with the inclusion of the electron mass the calculations are slower, but the code can be used for low beam energies and/or for backward scattering angles as large as 180°. The accuracy of HADES calculations can be improved well beyond the value quoted above at the expense of computational time by optimizing the accuracy parameters for the particular problem under consideration. The cross section accuracy can be checked by running HADES in a mode with $Z=0$; for this mode Coulomb distortion vanishes, and the results can be compared with those obtained from an analytically formulated plane-wave Born approximation (PWBA) calculation. The code can also analyze the convergence of its partial wave summations for each of the relevant transition amplitudes.

In HADES the electromagnetic interaction is treated in the Coulomb gauge. This has numerical advantages, and allows the identification of the numerically calculated DWBA amplitudes with the (retarded) magnetic or transverse electric and the (unretarded) charge transition amplitudes of the conventional analytic PWBA formulation. HADES includes most of the models used conventionally for the parametrization of the nuclear charge and current densities. It is particularly suited for "model-independent" evaluations of electron scattering data via Fourier-Bessel or oscillator function expansions of the nuclear charge distribution and of the transverse electric and/or the magnetic distributions. Model-independent evaluations can be performed conveniently with HADES by first calculating all relevant transition amplitudes for each term in the density expansion separately. These amplitudes are then used in a separate parameter-fitting routine to obtain the density expansion coefficients that provide a best fit to the experimental cross sections. This approach drastically reduces the total computing time required to fit typical electron scattering data.

APPENDIX B: DATA ANAYLSIS USING THE RIGID ROTOR MODEL

The low-lying level structure of ^{152}Sm is well described by a classical rotational model in which it is assumed that (1) the nuclear Hamiltonian can be separated into a rotational Hamiltonian and an intrinsic Hamiltonian that describes all other degrees of freedom; and (2) the nucleus has axial symmetry and reflection symmetry. Within the context of that model, the shape of the nuclear charge density in its intrinsic frame, $\rho(\mathbf{r})$, can be expanded in terms of spherical harmonics

$$\rho(\mathbf{r})=\sum_{\lambda}\sqrt{2\lambda+1}\rho_{\lambda a}(r)Y_{\lambda 0}(\Omega)\ . \tag{B1}$$

By inverting this equation, one obtains the (angular-averaged) ground state and transition charge densities:

$$\rho_{\lambda a}(r)=\frac{1}{\sqrt{2\lambda+1}}\int\rho(\mathbf{r})Y_{\lambda 0}(\Omega)d\Omega\ . \tag{B2}$$

The transition charge densities $\rho_{\lambda a}(r)$ for $\lambda=2,4,6,\ldots,$ in Eq. (B2) are identical to the $\rho_{\lambda}(r)$ defined in Eqs. (2)–(5), but the monopole term $\rho_{0a}(r)$ is normalized such that

$$4\pi\int\rho_{0a}(r)r^2dr=\sqrt{4\pi}Ze\ . \tag{B3}$$

This normalization is a factor of $\sqrt{4\pi}$ greater than the normalization traditionally used for the (angular-averaged) ground state charge density.

Two other conventions have been used in the analysis of electron scattering data from deformed nuclei at terms of the rigid rotor model. They both begin with the same assumptions outlined above. Bertozzi *et al.*[7] expand the density as

$$\rho(\mathbf{r})=\sum_{\lambda}\rho_{\lambda b}(r)Y_{\lambda 0}(\Omega)\ . \tag{B4}$$

Inverting this equation, they obtain a ground state and transition charge densities

$$\rho_{\lambda b}(r)=\int\rho(\mathbf{r})Y_{\lambda 0}(\Omega)d\Omega\ . \tag{B5}$$

With this convention the excitation probabilities are given by

$$B(E\lambda\uparrow)=\left|\int\rho_{\lambda b}(r)r^{\lambda+2}dr\right|^2\ , \tag{B6}$$

which differs by a factor of $(2\lambda+1)$ from the normalization commonly used in inelastic electron scattering [see Eq. (3) and Ref. 31]. The monopole term in this density expansion, $\rho_{0b}(r)$, is normalized identically to the $\rho_{0a}(r)$ in Eq. (B3).

A different expansion was used by Cardman *et al.*,[32]

$$\rho(\mathbf{r})=\sqrt{4\pi}\sum_{\lambda}\rho_{\lambda c}(r)Y_{\lambda 0}(\Omega)\ , \tag{B7}$$

implying

$$\rho_{\lambda c}(r)=\frac{1}{\sqrt{4\pi}}\int\rho(\mathbf{r})Y_{\lambda 0}(\Omega)d\Omega\ . \tag{B8}$$

With this convention the monopole term in the expansion is identical to the (angular-averaged) ground state charge density, but the transition charge densities are normalized such that

$$B(E\lambda\uparrow)=4\pi\left|\int\rho_{\lambda c}(r)r^{\lambda+2}dr\right|^2\ , \tag{B9}$$

which differs by a factor of $(2\lambda+1)/4\pi$ from the traditional normalization.

As is evident from the discussion above, it is not possible to arrive at a convention for the density expansion in the rigid rotor model that is consistent with the normalizations traditionally used in electron scattering for both the ground state and the transition charge densities. This (trivial) problem is a consequence of the normalizations of the spherical harmonic functions. For the present work, we have chosen to include the factor $\sqrt{2\lambda+1}$ in the expansion [see Eq. (B1)] so that the rigid rotor excited state densities have the normalization that is most commonly used for transition charge densities in electron scattering.

Early approaches[7,9] to the application of this model to electron scattering data involved the parametrization of the intrinsic shape of the charge distribution (for example, by employing a deformed Fermi distribution in which the half-density radius was expanded using a Legendre series) and determining the parameter values by simultaneously fitting the scattering data from the ground state rotational band. This simple model is adequate for the analysis of low momentum transfer electron scattering data, and has been used often to interpret data from Coulomb excitation and alpha-scattering experiments. However, this model has been shown[51] to be inadequate for the interpretation of electron scattering data for momentum transfers extending beyond 2 fm^{-1}.

Alternately, the transition charge densities inferred from "model-independent" fits to the scattering from each level may be combined[32] to infer the shape of the nuclear charge distribution in its intrinsic frame by substitution in Eq. (B1). This approach has the advantage that no bias on the intrinsic shape is introduced by the choice of a particular functional form for the charge distribution in the intrinsic frame. It must be mentioned,

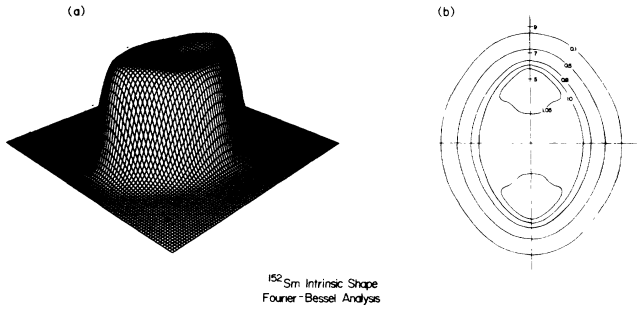

FIG. 10. The intrinsic shape of the ^{152}Sm charge density as inferred from the measured transition charge densities assuming rigid rotation: (a) a perspective view; and (b) constant charge density contours. The numbers on the contours are the density in units of the central density; the numbers on the axis are the distance from the origin in fm.

however, that the signs of the transition charge densities cannot be determined directly from inclusive electron scattering data. For the $\lambda=2$ density the sign is available from measurements of the hyperfine splitting in muonic atom spectra.[11,12] Measurements of the reorientation effect in Coulomb excitation[17–21] provide the sign of both the $\lambda=2$ and $\lambda=4$ densities. Unfortunately, the sign of the $\lambda=6$ density has not been determined experimentally. We have chosen a positive sign based on the theoretical description of the potential energy surface for ^{152}Sm discussed in Sec. IV. Figure 10 displays the intrinsic shape of the ^{152}Sm charge density obtained by inserting the measured $\lambda=0$, 2, 4, and 6 densities in Eq. (B1). The strong quadrupole and hexadecapole deformations of the ^{152}Sm ground state are clearly visible in the figure. The lobes observed in the density at ± 4 fm along the symmetry axis are a real feature of ^{152}Sm; they can be seen clearly in both the perspective view [Fig. 10(a)] and the contour map [Fig. 10(b)] of the density, and are not contained within the error band for the density.

[1]P. Leconte *et al.*, Nucl. Instrum. Methods **169**, 401 (1980).
[2]C. Grunberg and Ph. Leconte (unpublished).
[3]H. Ehrenberg *et al.*, Nucl. Instrum. Methods **105**, 253 (1972).
[4]S. Glückert and R. Neuhausen, Nucl. Instrum. Methods **151**, 509 (1978).
[5]W. Reuter, G. Fricke, K. Merle, and H. Miska, Phys. Rev. C **26**, 806 (1982).
[6]J. Bergstrom, in *Medium Energy Nuclear Physics*, MIT 1967 Summer Study, edited by W. Bertozzi and S. Kowalski (Massachusetts Institute of Technology, Cambridge, Massachusetts, 1967), p. 251.
[7]W. Bertozzi *et al.*, Phys. Rev. Lett. **28**, 1711 (1972).
[8]L. S. Cardman, D. Kalinsky, J. R. Legg, R. Yen, and C. K. Bockelman, Nucl. Phys. **A216**, 285 (1973).
[9]T. Cooper, W. Bertozzi, J. Heisenberg, S. Kowalski, W. Turchinetz, C. Williamson, L. Cardman, S. Fivozinsky, J. Lightbody, Jr., and S. Penner, Phys. Rev. C **13**, 1083 (1976).
[10]A. Nakada, N. Haik, J. Alster, J. B. Bellicard, S. Cochavi, B. Frois, M. Huet, P. Leconte, P. Ludeau, M. A. Moinester, and Phan Xuan Ho, Phys. Rev. Lett. **38**, 584 (1977).
[11]Y. Yamazaki, E. B. Shera, M. V. Hoehn, and R. M. Steffen, Phys. Rev. C **18**, 1474 (1978).
[12]R. J. Powers, P. Barreau, B. Bihoreau, J. Miller, J. Morgenstern, J. Picard, and L. Roussel, Nucl. Phys. **A316**, 295 (1979).
[13]K. W. Ford and G. A. Rinkler, Jr., Phys. Rev. C **7**, 1206 (1973).
[14]H. E. Wohlfahrt *et al.*, Phys. Rev. C **22**, 264 (1980).
[15]W. Reuter, E. B. Shera, H. D. Wohlfahrt, and Y. Tanaka, Phys. Lett. **124B**, 293 (1983).
[16]L. K. Wagner, E. B. Shera, G. A. Rinkler, and R. K. Sheline, Phys. Rev. C **16**, 1549 (1977).
[17]W. Bruckner, J. G. Merdinger, D. Pelte, U. Smilansky, and K. Traxel, Phys. Rev. Lett. **30**, 57 (1973).
[18]H. Fischer, D. Kamke, H. J. Kittling, E. Kuhlmann, H. Plicht, and R. Schormann, Phys. Rev. C **15**, 921 (1977).
[19]T. K. Saylor, J. X. Saladin, I. Y. Lee, and K. A. Erb, Phys. Lett. **42B**, 51 (1972).
[20]A. H. Shaw and J. S. Greenberg, Phys. Rev. C **10**, 263 (1974).
[21]H. J. Wollersheim, W. Wilcke, and Th. W. Elze, Phys. Lett. **48B**, 323 (1974).
[22]B. Frois, Nucl. Phys. **A358**, 383c (1981).
[23]D. G. Ravenhall, R. Herman, and B. C. Clark, Phys. Rev. **B136**, 589 (1964). The present version of this code has been revised extensively by S. E. Williamson (private communication).
[24]H. G. Andresen, M. Mueller, H. J. Ohlbach, and H. Peter, in International Conference on Nuclear Physics with Electromagnetic Interactions, Mainz, 1979. Abstracts of Contributed Papers 8.1.
[25]M. Mueller, Diplomarbeit, Institute for Nuclear Physics, University of Mainz, 1977.
[26]M. Mueller, Ph.D. thesis, Institute for Nuclear Physics, University of Mainz, 1984.
[27]H. J. Ohlbach, Diplomarbeit, Institute for Nuclear Physics, University of Mainz, 1981.
[28]H. G. Andresen, M. Engel, M. Mueller, and H. J. Ohlbach, Nucl. Phys. **A358**, 365 (1981).
[29]E. Wuest, U. Mosel, J. Kunz, H. G. Andresen, and H. Mueller, Nucl. Phys. **A402**, 235 (1983).
[30]H. Rothhaas, J. Friedrich, K. Merle, and B. Dreher, Phys. Lett. **51B**, 23 (1974).
[31]J. Heisenberg, Adv. Nucl. Phys. **12**, 61 (1981).
[32]L. S. Cardman, D. H. Dowell, R. L. Gulbranson, D. G. Ravenhall, and R. L. Mercer, Phys. Rev. C **18**, 1388 (1978).
[33]R. L. Mercer and D. G. Ravenhall, Phys. Rev. C **10**, 2002 (1974).
[34]R. L. Mercer, Phys. Rev. C **15**, 1786 (1977).
[35]D. G. Ravenhall and R. L. Mercer, Phys. Rev. C **13**, 2324 (1976).
[36]H. Flocard, P. Quentin, A. A. Kerman, and D. Vautherin, Nucl. Phys. **A203**, 433 (1973).
[37]J. Decharge, M. Girod, and D. Gogny, Phys. Lett. **55B**, 361 (1975).
[38]J. Negele and G. Rinker, Phys. Rev. C **15**, 1499 (1977).
[39]M. Girod and B. Grammaticos, Phys. Rev. Lett. **40**, 361 (1978).
[40]M. Girod and B. Grammaticos, Phys. Rev. C **27**, 2317 (1983).
[41]A. Bohr, K. Dan. Vidensk, Selsk. Mat. Fys. Medd. **26**, No. 14 (1952).
[42]K. Kumar, in *The Electromagnetic Interaction in Nuclear Spectroscopy*, edited by W. D. Hamilton (North-Holland, Amsterdam, 1975).
[43]M. Girod and B. Grammaticos, Nucl. Phys. **A330**, 40 (1979).
[44]D. R. Inglis, Phys. Rev. **103**, 1786 (1956).
[45]K. Kumar and M. Baranger, Nucl. Phys. **A92**, 608 (1967).
[46]A. Zaringhalam and J. W. Negele, Nucl. Phys. **A288**, 417 (1977).
[47]J. Decharge and D. Gogny, Phys. Rev. C **21**, 1568 (1980).
[48]J. F. Berger, M. Girod, and D. Gogny, Nucl. Phys. **A428**, 23c (1984).
[49]S. T. Belyavev, K. Dan. Vidensk, Selsk. Mat. Fys. Medd. **31**, No. 11 (1959).
[50]D. R. Yennie, D. G. Ravenhall, and R. N. Wilson, Phys. Rev. **95**, 500 (1954).
[51]R. Hoffman, Ph.D. thesis, Institute for Nuclear Physics, University of Mainz.
[52]J. R. Legg, Ph.D. thesis, Yale University, 1972.

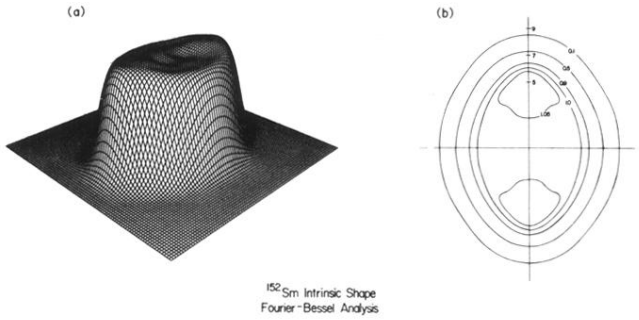

FIG. 10. The intrinsic shape of the ^{152}Sm charge density as inferred from the measured transition charge densities assuming rigid rotation: (a) a perspective view; and (b) constant charge density contours. The numbers on the contours are the density in units of the central density; the numbers on the axis are the distance from the origin in fm.

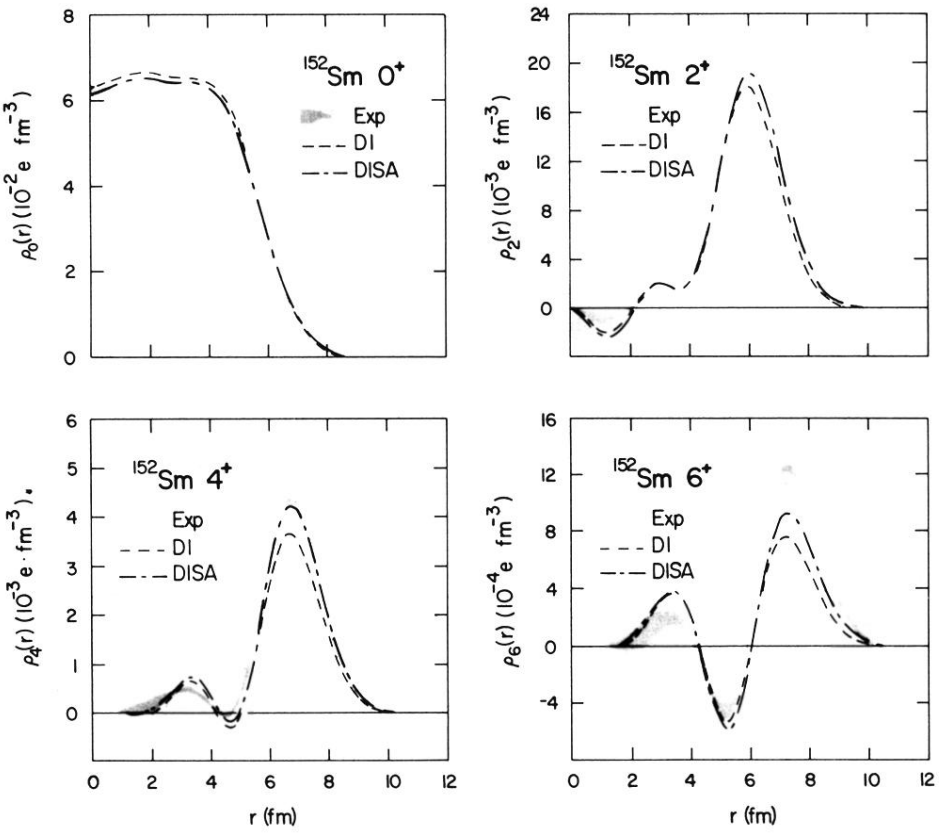

FIG. 8. The experimentally determined ground state and transition charge densities for the first four states of the ground state rotational band. Also shown are the theoretical predictions obtained using the $D1$ (— — —) and $D1SA$ (—·—·—·) effective interactions.

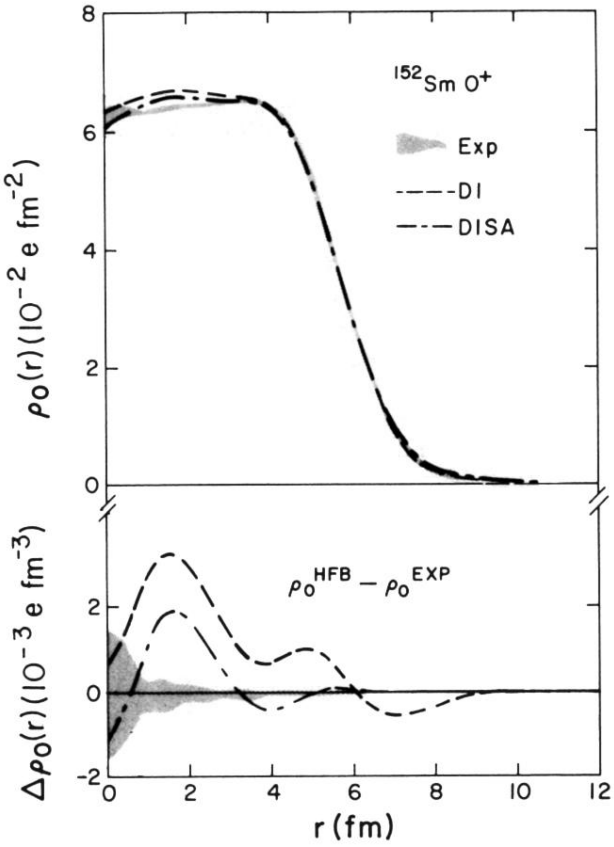

FIG. 9. The experimentally determined ground state charge density for ^{152}Sm and its uncertainty compared with the densities calculated using the *D*1 and *D*1*SA* effective interactions (a). Also shown are the differences between the experimental and theoretical densities (b).